How to cite: *Angew. Chem. Int. Ed.* **2020**, *59*, 15226–15231
International Edition: doi.org/10.1002/anie.202006486
German Edition: doi.org/10.1002/ange.202006486

Chirality

# Enantiomeric Discrimination by Surface-Enhanced Raman Scattering–Chiral Anisotropy of Chiral Nanostructured Gold Films

*Zexi Liu[+], Jing Ai[+], Prashant Kumar[+], Enming You[+], Xiong Zhou[+], Xi Liu[+], Zhongqun Tian, Petr Bouř, Yingying Duan,* Lu Han,* Nicholas A. Kotov,* Songyuan Ding,* and Shunai Che**

***Abstract:*** *A surface-enhanced Raman scattering-chiral anisotropy (SERS-ChA) effect is reported that combines chiral discrimination and surface Raman scattering enhancement on chiral nanostructured Au films (CNAFs) equipped in the normal Raman scattering Spectrometer. The CNAFs provided remarkably higher enhancement factors of Raman scattering (EFs) for particular enantiomers, and the SERS intensity was proportional to the enantiomeric excesses (ee) values. Except for molecules with mesomeric species, all of the tested enantiomers exhibited high SERS-ChA asymmetry factors (g), ranging between 1.34 and 1.99 regardless of polarities, sizes, chromophores, concentrations and ee. The effect might be attributed to selective resonance coupling between the induced electric and magnetic dipoles associated with enantiomers and chiral plasmonic modes of CNAFs.*

Enantiomeric discrimination is of critical importance in many areas of analytical sciences, chemical biology, pharmacy, and pesticide science.[1] Multiple theoretical concepts and chiroptical spectroscopic techniques, such as optical rotation and circular dichroism, have been developed to detect and quantify enantiomers. Typically, circularly polarized light is used to identify the absolute configuration and composition of enantiomers (Supporting Information, Table S1).[2] However, these methods are impossible to use for racemates or compounds with weak optical response.[3]

Surface-enhanced Raman spectroscopy is a powerful technique that provides ultra-sensitive structural information through the vibrational fingerprint of trace analytes,[4] owing to the interaction of molecules with the strong electromagnetic field[5] localized around metallic nanostructures which also contributes to strong radiation enhancement. The polarized analogue of SERS, surface-enhanced Raman optical activity (SEROA), was also proposed as a technique to identify enantiomers, using difference in SERS of left- and right-handed circularly polarized light (Supporting Information, Figure S1). However, similar to other methods employing OA (Supporting Information, Table S1), SEROA[6] provides relatively weak anisotropic signal (ROA/Raman ratio), and is useless for racemates.

We investigate a different approach, where the chiral anisotropy is created by a highly polarizable chiral platform that can discriminate enantiomers via SERS using linearly polarized or unpolarized light (Figure 1a; Supporting Information, Figure S1). The described SERS-ChA method is, thus, based on a selective SERS EF of enantiomers on

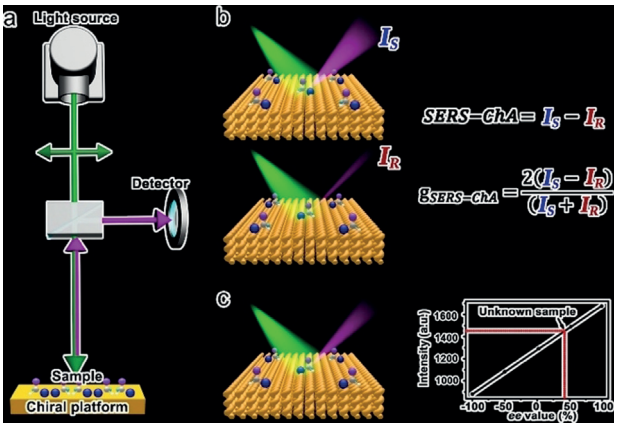


***Figure 1.*** Illustration of the SERS-ChA method for enantiomer discrimination. a) Conventional Raman scattering equipment with a chiral platform. b) SERS-ChA and *g*-factor are obtained for enantiomeric molecules. c) Absolute configurations and *ee* values of unknown samples can be obtained from the calibration curves.

[*] Z. Liu,[+] J. Ai,[+] Dr. Y. Duan, Prof. L. Han, Prof. S. Che
School of Chemical Science and Engineering, Tongji University
1239 Siping Road, Shanghai, 200092 (P. R. China)
E-mail: yyduan@tongji.edu.cn
luhan@tongji.edu.cn
chesa@tongji.edu.cn
Homepage: http://che.tongji.edu.cn
Prof. S. Che
School of Chemistry and Chemical Engineering
State Key Laboratory of Metal Matrix Composites
Shanghai Jiao Tong University
800 Dongchuan Road, Shanghai, 200240 (P. R. China)
Dr. P. Kumar,[+] Prof. N. A. Kotov
Department of Chemical Engineering and Biointerfaces Institute
University of Michigan, Ann Arbor, MI 48019 (USA)
E-mail: kotov@umich.edu
E. You,[+] Prof. Z. Tian, Prof. S. Ding
College of Chemistry and Chemical Engineering
Xiamen University, Xiamen, 361005 (P. R. China)
E-mail: syding@xmu.edu.cn
Dr. X. Zhou,[+] Dr. X. Liu[+]
SynCat@Beijing, Synfuels China Technology Co., Ltd
Beijing 101407 (P. R. China)
Prof. P. Bouř
Institute of Organic Chemistry and Biochemistry
Czech Academy of Sciences
Fleminovo náměstí 2, 16610 Prague (Czech Republic)
[+] These authors contributed equally to this work.
Supporting information and the ORCID identification number(s) for the author(s) of this article can be found under: https://doi.org/10.1002/anie.202006486.

  

a chiroplasmonic surface, which provides high enantiomeric sensitivity (Figure 1b). Observable parameters in SERS-ChA are defined as the difference in SERS intensities of enantiomeric molecules on the same chiral platform, SERS-ChA = $I_S - I_R$, where $I_S$ and $I_R$ are SERS intensities of *S*- and *R*-enantiomers, respectively (Figure 1b). The *g*-factor is defined in a usual way, as $g_{SERS\text{-}ChA} = 2(I_S - I_R)/(I_S + I_R)$. The maximum $\lim |g|_{max} = 2$ indicates a complete discrimination of enantiomers. Detecting and quantifying an unknown sample (Figure 1c) require a calibration curve, obtained for enantiomers as Raman intensity dependent of the *ee* values from −100% to +100% at known concentrations. The *g*-factor can be obtained from the slope ($k$) and intercept ($b$) of curve: $g_{SERS\text{-}ChA} = 2k/b$. The tested compound is then diluted to the concentration employed in the SERS-ChA standard curve to determine the Raman intensity and the corresponding *ee* value on the chiral plasmonic platform. The enantiomeric resolution system with SERS-ChA overcome the disadvantages of SEROA[7] (Supporting Information, Figure S1). It can also be used for any enantiomers regardless of their electric dipole, size, and functionality, which often problematic for chiral chromatography.

Herein, we fabricated a chiral platform for SERS-ChA consisting of arrays of CNAFs on various silicon-containing wafers, such as single-crystal silicon [Si (100)], quartz, and glass, via an amino acid-induced symmetry-breaking route (Supporting Information, Figure S2). The wafer was lithographically ablated to generate cylindrical holes (Supporting Information, Figure S2a,b) that served as sample cells for the quantitative detection of enantiomeric compounds in solution. The helical Au fibers were prepared in four steps by direct epitaxial growth on the substrate surface. First, the substrate was first activated using a $H_2SO_4/H_2O_2$ mixture with an abundance of silanol groups on the surface (Supporting Information, Figure S2c). Second, amino groups were modified to the surface via condensation of the silanols and the siloxane of 3-aminopropyltriethoxysilane to terminate the substrate surface (Supporting Information, Figure S2d). Third, a gel mixture composed of N-acetyl-L/D-cysteine (S/R-NAC), 4-mercaptobenzoic acid (4-MBA), $HAuCl_4$, (2*S*,3*R*)-ascorbic acid (AA), and $H_2O$ was subsequently introduced onto the substrate. 4-MBA acts as a coating agent, and AA reduces $Au^{3+}$ ions to $Au^0/Au^+$ during the helical growth of chiral Au nanofiber arrays on the wafer to form as-prepared CNAFs (Supporting Information, Figure S2e). The S/R-NAC would act as a symmetry-breaking agent in the helical fiber growth because the asymmetric arrangement of Au-S, Au-$NH_2$, and Au-COO bonds around the chiral carbon center regulates the Au crystal morphology. Moreover, CNAFs could not be obtained using the same fabrication route in the absence of NAC. The fiber growth followed a seed-mediated (Supporting Information, Figure S3) growth process through reducing Au at the interface between substrate and seeds.[8] Fourth, organic components were removed via electrochemical oxidation to produce chiral platforms of pure inorganic CNAFs (Supporting Information, Figures S2f, S4), which was confirmed by Raman spectroscopy (Supporting Information, Figure S5). *S*- and *R*-NAC enantiomers led to right-handed CNAFs (*R*-CNAFs) and left-handed CNAFs (*L*-CNAFs), respectively, which were confirmed from their structural orientation and their different responses to circularly polarized light (see below).

Figure 2a shows scanning electron microscopy (SEM) images of R-CNAFs grown on a Si (100) wafer with lithographically ablated cylinder holes. The films consist of densely packed Au nanofibers with a uniform length of about 500 nm

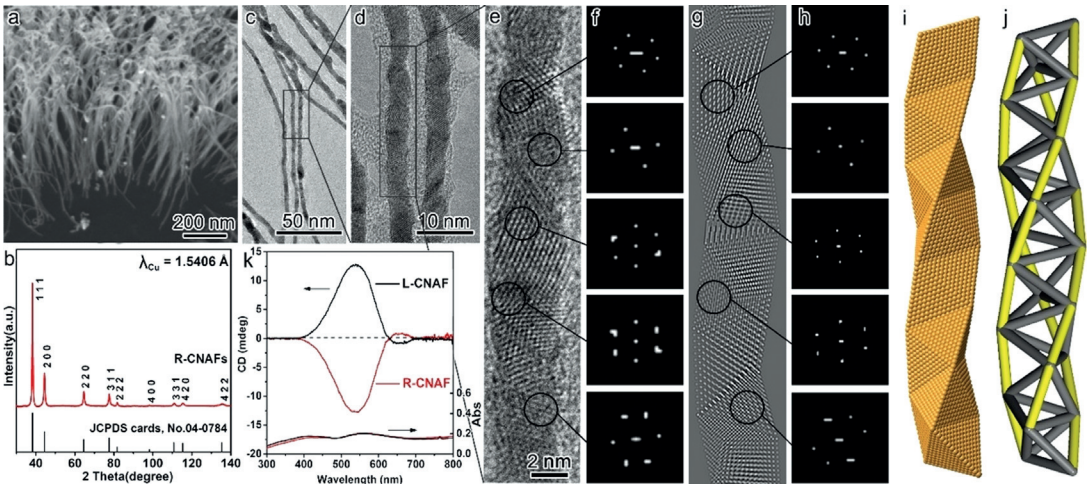


***Figure 2.*** Morphologies and structures of R-CNAFs. a) Low-magnification SEM image of Au nanofibers vertically grown on a Si wafer. b) The XRD pattern demonstrates that the Au crystals display a *fcc* structure and preferably grow along the ⟨111⟩ direction. c) Low-magnification TEM images of Au nanofibers that were mechanically removed from the wafer, showing twisting in almost all fibers. d) High-magnification TEM image of Au nanofibers showing a polycrystalline structure. e),f) HRTEM image and corresponding FDs of an Au fiber with an ideal BCB structure. g),h) Simulated TEM image and FDs showing good agreement with experimental observations. i) Representation of a right-handed chiral Au fiber, showing the BCB helix configuration from multiply twinned tetrahedral Au nanocrystals with a face-sharing relationship. j) A triple helix is revealed by connecting the outside edges of the stacked tetrahedra (yellow line). The synthetic chemical molar composition of R-CNAF was S-NAC/4-MBA/$HAuCl_4$/AA = 15:8:25:40. Note: The shadowed area around the fiber in the TEM image is the shrunk carbon film under electron beam irradiation (see the Supporting Information, Figure S8 for the shrinking process).

  

grown vertically on the surface of the silicon substrate. The crystalline structure of R-CNAF was analyzed by wide-angle X-ray diffractometry (XRD; Figure 2b). The reflections indicate that *R*-CNAF adopts the typical face-centered cubic (*fcc*) structure of Au in the space group $Fm\bar{3}m$ (JCPDS 04-0784) without any additional peaks. The relative intensity of {111} is much higher in *R*-CNAFs than in the bulk sample, suggesting the preferred orientation along the ⟨111⟩ direction in the Au fibers and dominance of {111} planes formed by the stacking of the tetrahedral Au nanoparticles (see below).

A low-magnification transmission electron microscopy (TEM) micrograph (Figure 2c) shows that almost all of the Au nanofibers present a helically twisting-like morphology and uniform diameters of about 5.5 nm. These helical nanofibers display a polycrystalline structure at high magnification (rectangular area, Figure 2c,d). The high-resolution TEM (HRTEM) image of a single Au nanofiber (Figure 2e) indicates that the tetrahedral units of the Au nanocrystals stacked into a so-called Boerdijk–Coxeter–Bernal (BCB) tetrahelix.[9] The surface energy of *fcc* crystals, such as Au, follows the order $\gamma\{111\} < \gamma\{100\} < \gamma\{110\}$. Therefore, the octahedral or tetrahedral shape is preferred to maximize the exposure of {111} facets. In the current work, the Au nanocrystals also have a tetrahedral shape, and the nanofibers consist of stacked tetrahedra that share their {111} facets in a multiply twinned manner. A right-handed in silico BCB model was built to interpret the helical structure: each tetrahedral nanocrystal is connected by twin boundaries that bind adjacent {111} facets (Figure 2i,j). The simulated HRTEM image[10] and the corresponding Fourier diffractograms (FDs) from different structural domains of the nanofiber show good agreement with the observed HRTEM images and the FDs (Figure 2e–h), which confirms that the structural model is realistic (Figure 2i and 2j). A few Au fibers also adopt imperfect BCB structures (Supporting Information, Figure S6). Perfect and imperfect tetrahelixes of *R*-CNAFs appear as right-handed triangular spirals. The *L*-CNAFs gave similar profiles with the same sizes and quality (Supporting Information, Figure S7). The handedness of antipodal CNAFs was also confirmed by their different responses to circular polarized light (see below).

The universality of the SERS-ChA effect was investigated by placing 100 pairs of commercially available enantiomers with different electric dipole configurations, sizes, chromophores, concentrations, and *ee* values (Supporting Information, Table S2) on R-CNAFs. Figure 3 shows the enantiomeric discrimination results of four typical enantiomeric compounds presenting at least one of the following properties: small or large molecular weight, low polarity, and chromophore-free structure, which are difficult to be applicable to chromatography or chiroptical spectroscopy. The four compounds were 2-butanol (Figure 3a), epichlorohydrin (Figure 3b), limonene (Figure 3c), and 2,2-dimethyl-α,α,α′,α′-tetra(1-naphthyl)-1,3-dioxolane-4,5-dimethanol (Figure 3d).

As a typical example, the Raman spectra of 2-butanol were compared for *ee* values varying from −100% to +100% (Figure $3a_1$). All peak areas for characteristic Raman scattering of enantiomers show good linear correlations with the *ee* value (Figure $3a_2$; Supporting Information, Figure $S9a_1$). SERS intensities of *S*-enantiomers are nearly two orders of magnitude higher than those of their *R* analogues, indicating highly selective SERS enhancement of antipodal enantiomers on *R*-CNAFs. The normalized linear curves for each scattering peak show identical trend, a linear correlation between each SERS peak area and the *ee* value (Supporting Information, Figure $S9a_2$). The *g*-factor of antipodal 2-butanol on *R*-CNAFs was $1.87 \pm 0.02$ obtained from the slopes of calibration curves using each detectable Raman peak area (Supporting Information, Figure $S9a_1$), which reveals fundamentally different Raman scattering behavior between two enantiomers and the same selectivity for all vibrational bands. The other three sets of model enantiomers exhibit a similar correlation between SERS signals and *ee* values, with high *g*-factors of 1.90, 1.95, and 1.85 (Figure 3b–d; Supporting Information, Figure S9b–d). With the exception of the molecules displaying the same amounts of mesomeric species, 98 pairs of the 100 enantiomers can be discriminated with high *g*-factors ranging from 1.34–1.99 (Supporting Information, Table S2), indicating the high discrimination capacity of

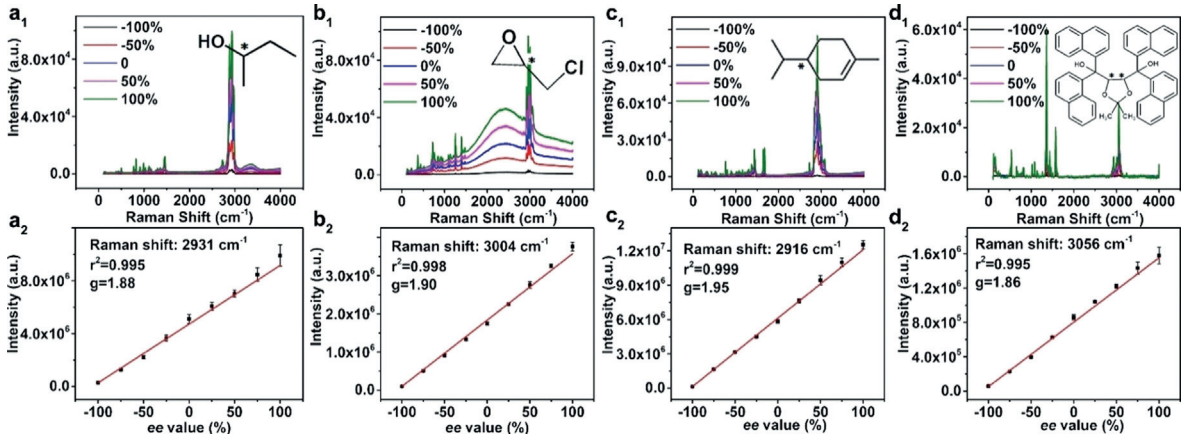


***Figure 3.*** Examples of the SERS-ChA effect of R-CNAFs. Raman spectra (top) and dependencies (bottom) of the largest SERS peak areas on *ee* values, from −100% to +100% for four sets of enantiomers. $a_1$),$a_2$) 2-butanol (MW 74.1). $b_1$),$b_2$) epichlorohydrin (MW 92.5). $c_1$),$c_2$) limonene (MW 136.2). $d_1$),$d_2$) 2,2-dimethyl-α,α,α′,α′-tetra(1-naphthyl)- 1,3-dioxolane-4,5-dimethanol (DTNDD) (MW 666.8).

  

CNAFs. The *g*-factors seem independent of any molecular features, including size, nature, and number of functional groups, electric dipole configuration, and presence of chromophores. The SERS-ChA effect of CNAFs could be efficient over a wide range of *ee*.

The specimen loading amount per unit area was optimized to eliminate the influence of molecular amounts on the surface so that the SERS intensity expresses the intrinsic properties of CNAFs. This optimization was performed by measuring the *g*-factor and SERS intensity for different enantiomer loading amounts ranging between $2.5\times10^{-11}$ and $7.5\times10^{-6}$ mol mm$^{-2}$ (Supporting Information, Figure S10) The measured *g*-factors remained almost constant at loading rates ranging from $2.5\times10^{-9}$ to $7.5\times10^{-8}$ mol mm$^{-2}$ while the SERS intensity remained high between $2.5\times10^{-9}$ and $2.5\times10^{-8}$ mol mm$^{-2}$ for the four types of enantiomers. This indicates that having an inadequate or an excess number of molecules outside the CNAFs decreases the accuracy of its discrimination, as expected. To ensure a high signal-to-noise ratio and clear SERS-ChA effect on CNAFs, SERS measurements were performed at a relatively high loading ($2.5\times10^{-8}$ mol mm$^{-2}$) and with constant *g*-factors. The consistency and homogeneity of the film, which ensure the accuracy of SERS-ChA, were confirmed for nine different films fabricated according to the same preparation parameters and nine different cylinder cells, respectively (Supporting Information, Figure S11, Tables S3, S4). The error of the *g*-factor for films and cylinder cells was 0.1 % and 0.2 %, respectively. Other tests indicate that the SERS-ChA effect is stable with respect to pH (Supporting Information, Figure S12), mixtures with achiral/ chiral interferences (Supporting Information, Figures S13, S14) and mixture enantiomers (Supporting Information, Figure S15), and reproducible (Supporting Information, Tables S3, S4) for a real-world sample.

The *g*-factors of both racemic CNAFs and achiral nanostructured Au films (NAFs) were zero (Supporting Information, Figure S16a,b) and that of L-CNAFs was negative (Supporting Information, Figure S16e). The enhancement in Raman intensities of R-CNAFs loaded with racemic molecules was 35 and 200 times greater than those of racemic CNAFs and achiral NAFs (Supporting Information, Figure S16e), respectively, which may be resulted from the large number of hot spots in chiral nanostructured Au fibers. The twisting of chiral molecules on the synthesis of Au nanofibers produced the chiral fiber structure and a multitude of crystalline defects that act as hot spots where Raman scattering can be substantially amplified. The sharp corners of the tetrahedral crystal units were also suggested playing a part in this phenomenon.[11]

The chemical adsorption and optical properties of CNAFs were analyzed to investigate the chiral discrimination mechanism. X-ray photoelectron spectroscopy (XPS) of R-CNAFs provided no peaks, indicating absence of organic compounds in *R*-CNAFs (Supporting Information, Figure S17). When *R*-CNAFs were loaded with *S*- and *R*-NAC, the XPS spectra showed peaks at approximately 400 eV, which is attributed to the N 1s of NAC. The peaks had almost identical areas, implying that equal amounts of antipodal NAC were adsorbed on the *R*-CNAF surface, which indicates no enantiomeric selectivity upon chemical adsorption in *R*-CNAF.

The SERS selectivity of SERS-ChA effect of one enantiomers over the other counterparts can be evidenced by ultraviolet-visible (UV/Vis) and circular dichroism (CD) spectra. Figure 4a shows the UV/Vis and CD spectra of antipodal CNAFs grown on transparent quartz wafer. Experimental mirror-imaged CD spectra of *R*- and *L*-CNAF reflected the selective interaction between the CNAFs and circularly polarized light due to the dissymmetric centers existing in the plasmonic resonance state of CNAFs. The transmitted CD (TCD) spectra of antipodal CNAFs exhibited opposite signals at about 514 nm originated from both scattering-based OA (SOA) and plasmonic absorption-based OA (AOA; Supporting Information, Figure S18a). It is known that the diffuse-reflection CD with white ($DRCD_W$) and black ($DRCD_B$) background approximately show the solely AOA and both SOA and AOA, because almost all light would be reflected by white and absorbed by black background; and the signals of SOA with white and black background are opposite because transmitted and reflected light were detected by the TCD and DRCD system, respectively (Supporting Information, Figure S18b,c). The $DRCD_W$ spectrum of *R*-CNAF displayed a positive coupling

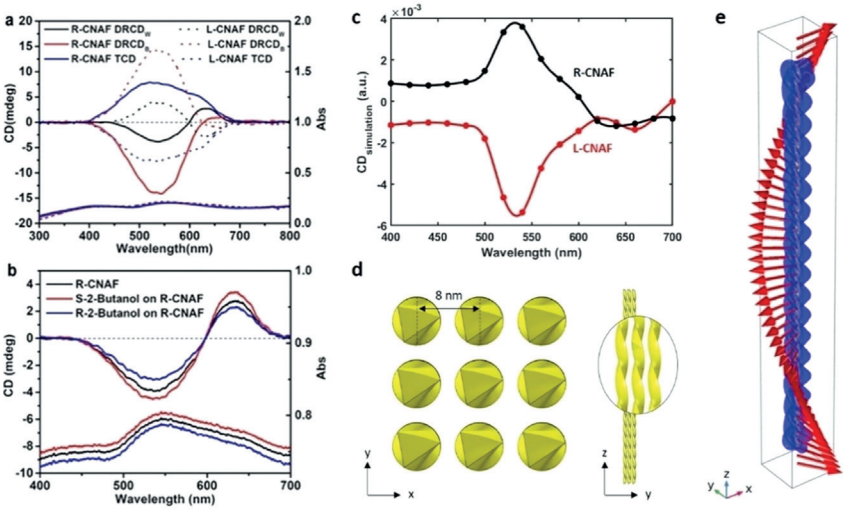


***Figure 4.*** Selective enhancement of resonance between CNAFs and enantiomers. a) UV/Vis and CD spectra of antipodal CNAFs grown on quartz substrate measured with TCD and $DRCD_W$ and $DRCD_B$, respectively. b) Diffuse-reflection UV/Vis with white background ($DRUV\text{-}Vis_W$) and $DRCD_W$ spectra of R-CNAFs and loading with *S*- and *R*-2-butanol. c) Simulated differential extinction cross-section for modeled L- and R-tetrahelices. d) Geometry of modeled tetrahelices to mimic experimental conditions with diameter of helices set as 5 nm and the center-center separation of 8 nm with a length of 400 nm. e) Spatial distribution of scattered electric field (blue isosurface at $6.6\times10^8$ V m$^{-1}$) around a modeled left-handed helix (yellow) in left-handed circularly polarized electric field (red arrows) of wavelength 460 nm.

centered at about 600 nm originated from the plasmonic absorption of CNAFs with right-handedness. Therefore, the TCD spectra can be considered as a combination of positive SOA and positive AOA (Supporting Information, Figure S19a); and the $DRCD_B$ spectra shows the combination of negative SOA and analogical positive AOA (Supporting Information, Figure S19c); which confirmed again the right-handedness of *R*-CNAFs. The CD spectra showed such small circular polarization excess arising from antipodal CNAF that it can be negligible as circularly polarized incident light for SEROA. Thus, the circular polarization does not contribute to the SERS-ChA effect.

The selective enhancement of localized electromagnetic fields generated by different interaction between enantiomeric molecules and CNAFs were confirmed by $DRUV\text{-}Vis_W$ and DRCDW spectra of antipodal enantiomers loaded on *R*-CNAF. Compared to the raw *R*-CNAF, both plasmonic absorbance and corresponding $DRCD_W$ signal of *R*-CNAF were enhanced with loading *S*-2-butanol while weakened with *R*-2-butanol (Figure 4b), which confirmed the selective enhancement of localized optical field owing to the more intensive resonance between *R*-CNAF and *S*-2-butanol over *R*-2-butanol. The generated Raman spectra of enantiomers were further enhanced by the local chiral electromagnetic field of *R*-CNAFs leading to SERS-ChA effect. Other three pairs of enantiomers shown in Figure 2 also displayed similar chiral-selective enhancement resonance between enantiomers and R-CNAFs (Supporting Information, Figure S20).

By analogy to the electromagnetic theory of conventional SERS[5] and previous studies on plasmonic enhancement of vibrational spectra,[12] the SERS-ChA on *R*-CNAF originate from the local chiral electromagnetic fields (Figure 4e) that interact asymmetrically with *R*- and *S*- enantiomers. The match between experimental and calculated CD spectra (Figure 4c,d; Supporting Information, Figures S21, S22) validate the electromagnetic filed calculations and give additional evidence for strong asymmetry of the local fields in *R*-CNAF platform. These local fields in the assemblies of nanowires (Figure 2a) enhance Raman scattering for both enantiomers but for one of them is substantially stronger due to the match with chirality of the molecules.

To the best of our knowledge, the SERS-ChA effect is the first example of efficient chiral response of pure inorganic materials used for determining the absolute configuration and enantiomeric excess. The system displays a versatility covering almost all enantiomers regardless of their polarity, size, and chromophore content, which is promising for enantiomeric discrimination technologies and open new horizons for chiral responses in chemistry, physics and biology. The effect also provides daunting challenges and opportunities in various research areas, such as chiral theory, chiroptical spectroscopy, asymmetric catalysis, chiral bio-response, and manufacturing of optical, electrical, and mechanical device developments.

## Acknowledgements

We thank Prof. Bin Ren, Yifan Bao, and Sisi Wu (Xiamen University), Prof. Yitao Long, Binbin Chen, and Jian Lv (East China University of Science and Technology). This work was supported by the National Natural Science Foundation of China (Grant No. 21931008 and 21533002, S.C.; 21975184, Y.D.; 21922304 and 21873072, L.H.; 21673273 and 21872163, X.L.), Science foundation of the Shanghai Municipal Science and Technology Commission (19JC1410300, S.C.), GAČR (18-05770S; P.B) and MŠMT (LTC17012; P.B.).

## Conflict of interest

The authors declare no conflict of interest.

**Keywords:** chiral anisotropy · chiral nanostructured Au film · chiral response · enantiomeric discrimination · surface-enhanced Raman scattering

[1] a) J. Shen, Y. Okamoto, *Chem. Rev.* **2016**, *116*, 1094–1138; b) T. D. James, K. Sandanayake, S. Shinkai, *Nature* **1995**, *374*, 345–347; c) D. Patterson, M. Schnell, J. M. Doyle, *Nature* **2013**, *497*, 475–478; d) K. Banerjee-Ghosh, O. Ben Dor, F. Tassinari, E. Capua, S. Yochelis, A. Capua, S. H. Yang, S. S. P. Parkin, S. Sarkar, L. Kronik, L. T. Baczewski, R. Naaman, Y. Paltiel, *Science* **2018**, *360*, 1331–1334; e) S. Dutta, A. J. Gellman, *Chem. Soc. Rev.* **2017**, *46*, 7787–7839; f) P. Lesot, C. Aroulanda, H. Zimmermann, Z. Luz, *Chem. Soc. Rev.* **2015**, *44*, 2330–2375.

[2] a) L. D. Barron, *Molecular Light Scattering and Optical Activity*, Cambridge University Press, Cambridge, **1982**; b) N. Berova, L. Di Bari, G. Pescitelli, *Chem. Soc. Rev.* **2007**, *36*, 914–931; c) L. Yang, C. S. Kwan, L. L. Zhang, X. H. Li, Y. Han, K. C. F. Leung, Y. G. Yang, Z. F. Huang, *Adv. Funct. Mater.* **2019**, *29*, 8; d) B. T. Thole, P. Carra, F. Sette, G. Vanderlaan, *Phys. Rev. Lett.* **1992**, *68*, 1943–1946; e) L. A. Nafie, *Vibrational Optical Activity: Principles and Applications*, Blackwell Science Publ, Oxford, **2011**; f) N. Berova, K. Nakanishi, R. W. Woody, *Circular dichroism : principles and applications*, Wiley-VCH, Weinheim, **2000**; g) N. Bouldi, N. J. Vollmers, C. G. Delpy-Laplanche, Y. Joly, A. Juhin, P. Sainctavit, C. Brouder, M. Calandra, L. Paulatto, F. Mauri, U. Gerstmann, *Phys. Rev. B* **2017**, *96*, 12.

[3] a) D. Sofikitis, L. Bougas, G. E. Katsoprinakis, A. K. Spiliotis, B. Loppinet, T. P. Rakitzis, *Nature* **2014**, *514*, 76–79; b) S. Beaulieu, A. Comby, D. Descamps, B. Fabre, G. A. Garcia, R. Geneaux, A. G. Harvey, F. Legare, Z. Masin, L. Nahon, A. F. Ordonez, S. Petit, B. Pons, Y. Mairesse, O. Smirnova, V. Blanchet, *Nat. Phys.* **2018**, *14*, 484–489.

[4] a) K. Kneipp, Y. Wang, H. Kneipp, L. T. Perelman, I. Itzkan, R. Dasari, M. S. Feld, *Phys. Rev. Lett.* **1997**, *78*, 1667–1670; b) S. Y. Ding, J. Yi, J. F. Li, B. Ren, D. Y. Wu, R. Panneerselvam, Z. Q. Tian, *Nat. Rev. Mater.* **2016**, *1*, 16; c) M. Fleischmann, P. J. Hendra, A. J. McQuillan, *Chem. Phys. Lett.* **1974**, *26*, 163–166.

[5] a) M. Moskovits, *Rev. Mod. Phys.* **1985**, *57*, 783–826; b) E. C. Le Ru, P. G. Etchegoin, *Principles of Surface-Enhanced Raman Spectroscopy*, Elsevier, Amsterdam, **2009**.

[6] S. Abdali, E. W. Blanch, *Chem. Soc. Rev.* **2008**, *37*, 980–992.

[7] L. D. Barron, A. D. Buckingham, *Annu. Rev. Phys. Chem.* **1975**, *26*, 381–396.

[8] J. He, Y. Wang, Y. Feng, X. Qi, Z. Zeng, Q. Liu, W. S. Teo, C. L. Gan, H. Zhang, H. Chen, *ACS Nano* **2013**, *7*, 2733–2740.

  

[9] a) Y. H. Zhu, J. T. He, C. Shang, X. H. Miao, J. F. Huang, Z. P. Liu, H. Y. Chen, Y. Han, *J. Am. Chem. Soc.* **2014**, *136*, 12746 – 12752; b) A. H. Boerdijk, *Philips Res. Rep.* **1952**, *7*, 303 – 313; c) J. Yan, W. C. Fang, J. Y. Kim, J. Lu, P. Kumar, Z. Z. Mu, X. C. Wu, X. M. Mao, N. A. Kotov, *Chem. Mater.* **2020**, *32*, 476 – 488.
[10] P. Oleynikov, *Cryst. Res. Technol.* **2011**, *46*, 569 – 579.
[11] a) J. Zhou, J. An, B. Tang, S. P. Xu, Y. X. Cao, B. Zhao, W. Q. Xu, J. J. Chang, J. R. Lombardi, *Langmuir* **2008**, *24*, 10407 – 10413; b) C. G. Khoury, T. Vo-Dinh, *J. Phys. Chem. C* **2008**, *112*, 18849 – 18859.
[12] M. Yang, R. Alvarez-Puebla, H. S. Kim, P. Aldeanueva-Potel, L. M. Liz-Marzan, N. A. Kotov, *Nano Lett.* **2010**, *10*, 4013 – 4019.

Manuscript received: May 5, 2020
Accepted manuscript online: May 18, 2020
Version of record online: June 21, 2020

  